ACS APPLIED MATERIALS & INTERFACES

Research Article

www.acsami.org

Achieving Enhanced Visible-Light-Driven Photocatalysis Using Type-II $NaNbO_3$/CdS Core/Shell Heterostructures

Sandeep Kumar,[†,‡] Sunita Khanchandani,[‡] Meganathan Thirumal,[†] and Ashok K. Ganguli*[,‡,§]

[†]Department of Chemistry, University of Delhi, New Delhi, Delhi 110007, India

[‡]Department of Chemistry, Indian Institute of Technology, Hauz Khas, New Delhi, Delhi 110016, India

[§]Institute of Nano Science & Technology, Habitat Centre, Phase-X, Sector-64, Mohali, Punjab 160062, India

Supporting Information

ABSTRACT: Expanding the light-harvesting range and suppressing the quick recombination of photogenerated charge carriers are of paramount significance in the field of photocatalysis. One possible approach to achieve wide absorption range is to synthesize type-II core/shell heterostructures. In addition, this system also shows great promise for fast separation of charge carriers and low charge recombination rate. Herein, following the surface functionalization method using 3-mercaptopropionic acid (MPA) as a surface functionalizing agent, we report on designing $NaNbO_3$/CdS type-II core/shell heterostructures with an absorption range extending to visible range and explore the opportunity toward degradation of methylene blue (MB) dye as a model pollutant under visible light irradiation. Characterizations including X-ray diffraction (XRD), field-emission scanning electron microscopy (FESEM), UV−vis diffuse reflectance spectrum (DRS), transmission electron microscopy (TEM), energy dispersive X-ray spectroscopy (EDS), and Raman spectroscopy support the growth of CdS shell onto $NaNbO_3$ nanorods. The resulting core/shell heterostructures unveiled high surface areas, enhanced light harvesting, and appreciably increased photocatalytic activity toward MB degradation compared to individual counterparts and the photocatalytic standard, Degussa P25, under visible light irradiation. The remarkably enhanced photocatalytic activity of core/shell heterostructures could be interpreted in terms of efficient charge separation owing to core/shell morphology and resulting type-II band alignment between $NaNbO_3$ and CdS, which creates a step-like radial potential favoring the localization of one of the carriers in the core and the other in the shell. A plausible mechanism for the degradation of MB dye over $NaNbO_3$/CdS core/shell heterostructures is also elucidated using active species scavenger studies. Our findings imply that hydroxyl radicals ($OH^•$) play a crucial role in dictating the degradation of MB under visible light. This work highlights the importance of core/shell heterostructures in leading toward new paradigms for developing highly efficient and reusable photocatalysts for the destructive oxidation of recalcitrant organic pollutants.

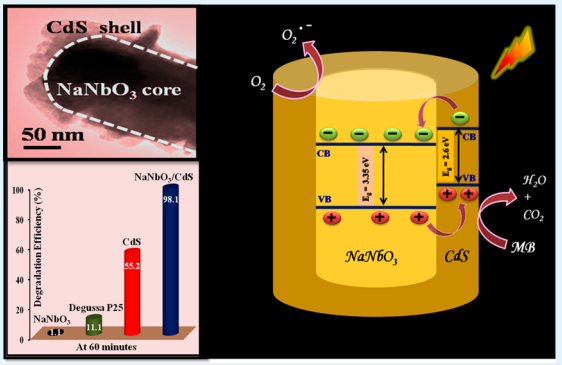

KEYWORDS: *$NaNbO_3$, CdS, photocatalysis, type-II band alignment, methylene blue, core/shell, heterostructures*

INTRODUCTION

Semiconductor photocatalysis has gained international eminence as a vanguard solution for the destructive oxidation of recalcitrant organic pollutants to mitigate the deterioration of environment.[1,2] Following the landmark work by Fujishima and Honda,[3] the semiconductor photocatalyst, TiO_2, has received intense scrutiny owing to its unsurpassed stability and efficiency. This milestone research opens up a new chapter in the field of photocatalysis and attempts to outperform TiO_2, having generated a large array of novel photocatalytic materials such as ZnO, SnO_2, $BiVO_4$, $SrTiO_3$, $NaNbO_3$, ZrO_2, WO_3, and so forth.[4−11] Among the explored semiconductor photocatalyst systems, perovskite based metal oxides[12−14] such as $SrTiO_3$ and $NaNbO_3$ have garnered noticeable attention in alleviating noxious pollutants and are touted as an environmentally benign and viable alternative to TiO_2. In this regard, sodium niobate ($NaNbO_3$), an intriguing material with a typical pervoskite structure and rich pool of useful properties including good chemical stability, high crystallinity, low cost, abundance, and low environmental impact has spurred a great deal of scientific and technological interest.[15−17] Nevertheless, the prospect of efficient photocatalysis has not been reached primarily due to the wide band gap associated with $NaNbO_3$ that precludes significant activity under visible light.[18,19] Another daunting issue still remains with $NaNbO_3$ in suppressing the rapid recombination of photoexcited charge carriers.[20] Thus, strenuous efforts have been devoted to push the absorption onset of $NaNbO_3$ toward longer wavelengths and to accelerate

Received: May 19, 2014
Accepted: July 15, 2014
Published: July 15, 2014

the separation of charge carriers for improving the degradation of pollutants under visible illumination.[18,21−23] In this context, of particular note is the construction of one-dimensional nanostructures (e.g., nanotube, nanowire, nanobelt, nanorod, etc.) which render a continuous electron-transport pathway for the fast collection of photoexcited carriers, thus retarding the recombination of charges leading to enhanced absorption and efficiency under visible light irradiation.[24,25] Another booming strategy to surmount the issue of high energy photons of wide band gap metal oxides is to integrate with low band gap semiconductors in a single nanostructured material.[26−28] Low band gap semiconductors such as metal chalcogenides (e.g., CdS, CdSe, PbSe, CdTe) exhibit discrete energy levels and size-tunable band gaps, which allow the design and tailoring for efficient light harvesting.[29] Such light harvesting capability coupled with the possibility of multiple exciton generation through size and composition modulation makes these semiconductors strong contenders for sensitizing wide band gap materials.[30−32] To date, as a well-known metal chalcogenide and II−VI semiconductor, CdS has been ubiquitously employed in light harvesting owing to its favorable band gap (2.4 eV), corresponding well with the spectrum of sunlight and suitable band edge positions and high extinction coefficient.[33−36] Thus, it is speculated that the sensitization property of CdS not only extends the response of $NaNbO_3$ nanostructures to the visible region but may also facilitate the charge suppression process. An additional potentially effective approach to modulate the spectral response of $NaNbO_3$ using CdS sensitizer is by adopting the core/shell strategy, which creates a step-like radial potential favoring the localization of one of the carriers in the core and the other in the shell.[37,38] The growth of CdS shell on $NaNbO_3$ core nanostructures results in a type-II band structure configuration of core/shell heterostructures,[39−43] which confers a platform for the separation of carriers through core/shell interface and allowing access to longer wavelengths. Thus, the judicious integration of $NaNbO_3$ with CdS sensitizers in core/shell systems offering enhanced charge separation and significantly improved photocatalytic activity through the deployment of a type-II band structure configuration is highly desired.

By building from these ideas, for the first time, type-II $NaNbO_3$/CdS core/shell heterostructures were synthesized using the surface functionalization route. Evaluated by the degradation of methylene blue (MB), these core/shell heterostructures offer superior photocatalytic activity compared to the corresponding single component and the photocatalytic standard, commercial TiO_2 (Degussa P25) under visible light irradiation. This enhancement could be related to the efficient transfer of photogenerated carriers and wide absorption range resulting from the type-II band gap structure and core/shell configuration. The stability of the as-synthesized core/shell heterostructures is further examined by monitoring the photocatalytic activity for three successive cycles of degradation. No appreciable loss in photocatalytic activity is observed and structural integrity is retained, as evidenced by X-ray diffraction studies even after three cycles of degradation, which predicts the stability and reusability of these core/shell heterostructures for practical use in environmental applications. To the best of our knowledge, this work is the first report of the synthesis and exploration of the photocatalytic activity of $NaNbO_3$/CdS core/shell heterostructures. We envisioned that our work may provide a straightforward paradigm for developing highly efficient, stable, and reusable core/shell heterostructures for environmental sustainability and energy-harvesting applications.

EXPERIMENTAL SECTION

Preparation of $NaNbO_3$ Nanorods. The utilized $NaNbO_3$ nanorods were fabricated by following the hydrothermal route.[44] In a typical synthesis, niobium pentoxide (Nb_2O_5) was dispersed in deionized water. The resulting solution was then mixed with 10 N NaOH solution and allowed to stir at room temperature for 2 h. The reaction mixture was then transferred to a 100 mL Teflon-lined stainless steel autoclave and heated at 150 °C for 48 h. Subsequently, the autoclave was allowed to cool down to room temperature naturally. The resulting products were collected by centrifugation, washed several times with deionized water and absolute ethanol, and finally dried at 70 °C for 4 h.

Preparation of CdS Nanoparticles. We have also conducted the hydrothermal method for the synthesis of CdS nanoparticles using cadmium nitrate tetrahydrate and thiourea as precursors.[45] Typically, cadmium nitrate tetrahydrate and thiourea were separately dissolved in 50 mL of ethylene glycol. Subsequently, the cadmium solution and the thiourea solution were mixed together and loaded in a 100 mL Teflon-lined stainless steel autoclave. The reaction mixture was heated at 180 °C for 2 h and then air-cooled to room temperature. The resulting yellow product was separated by centrifugation and washed repeatedly with deionized water and absolute ethanol.

Preparation of $NaNbO_3$/CdS Core/Shell Heterostructures. For the growth of CdS shell onto $NaNbO_3$ nanorods, we adopted a surface functionalization route using 3-mercaptopropionic acid (MPA) as the functionalizing agent.[46] 20 μL of MPA was added to the $NaNbO_3$ nanorods dispersed in water and the reaction mixture was allowed to stir for 4 h at room temperature to completely functionalize the surface of nanorods. Afterward, $Cd(NO_3)_2{\cdot}4H_2O$ solution was added gradually drop by drop to the above reaction mixture under constant magnetic stirring at room temperature. Finally, $Na_2S{\cdot}9H_2O$ was added slowly to the system and stirred constantly at room temperature. The solution gradually turned to a faded yellow color, suggesting the formation of CdS layer over $NaNbO_3$ nanorods. The resulting yellow colored product was extracted by centrifugation and washed repeatedly with water and absolute alcohol.

Characterization. *X-ray Diffraction (XRD).* The crystallinity, phase composition, and purity of the resulting products were assessed through X-ray diffraction (XRD) analysis on a Bruker D8 Advance diffractometer equipped with Ni-filtered Cu Kα radiation (λ = 1.5418 Å) in the 2θ range of 10−70° at a scanning rate of 0.02° per second.

The strain developed during the shell formation was estimated by Williamson-Hall plot using the following equation[47]

$$\beta\cos\theta/\lambda = 1/D + \eta \sin\theta/\lambda \quad (1)$$

where β is the full width at half-maximum (fwhm) of the θ−2θ peak, θ is the diffraction angle, λ is the X-ray wavelength, η is the effective strain, and D is the crystallite size. The strain (η) is calculated from the slope and the crystallite size (D) is calculated from the intercept of a plot of β cos θ/λ against sin θ/λ.

The crystallite sizes obtained using Williamson-Hall plot were corroborated with the crystallite sizes (D_{Sch}, in Å) calculated by the application of the Scherrer's formula (eq 2) to the PXRD data:[48]

$$D_{Sch} = K\lambda/\beta \cos\theta \quad (2)$$

where λ is the wavelength of Cu Kα radiation, β is the corrected half-width of the diffracted peak, θ is the diffraction angle, and K is equal to 0.9.

Raman Spectroscopy. Raman spectra of the as-synthesized samples in the powder form were recorded at room temperature with a Horiba Xplora micro-Raman system equipped with a 532 nm Ar^+ ion laser. To avoid excessive heating during measurements, the powder samples were recorded at a laser power of 3 mW.

Field-Emission Scanning Electron Microscopy (FESEM). The surface morphologies of all the synthesized samples were analyzed with the aid of field-emission scanning electron microscopy (FEI

QUANTA 3D FEG) operating at an accelerating voltage of 5 kV equipped with an energy dispersive X-ray spectroscopy (EDS) detector for elemental mapping. A small amount of dry sample was put on carbon tape adhered to an aluminum stub and sputter-coated by an ultrathin layer of gold prior to inspection to prevent sample-charging effects and observed at magnifications 20 000 times their original size.

Transmission Electron Microscopy (TEM), High Resolution TEM (HRTEM), and Point EDS. TEM and HRTEM studies were employed to gain detailed insight into the morphology of the as-synthesized core/shell heterostructures. Specimens for TEM investigations were prepared by first dispersing the as-synthesized samples in ethanol under the assistance of ultrasonication and then dropping one drop of the suspension onto a 400-mesh copper grid, coated with a holey carbon film. Images were recorded on a FEI Technai G^2 20 operated at an accelerating voltage of 200 kV. This instrument was equipped with an energy dispersive X-ray spectroscopy (EDS) system with the potential of performing point EDS scan from the edge and the center of the heterostructures to further substantiate the core/shell formation in $NaNbO_3$/CdS heterostructures.

UV–vis Diffuse Reflectance Spectra (UV–vis DRS). The optical properties of as-synthesized samples in the pressed disk form were analyzed by UV–vis diffuse reflectance spectroscopy recorded on a Shimadzu UV-2450 spectrometer equipped with an integrating sphere assembly, over a wavelength range of 250–700 nm employing $BaSO_4$ as a reflectance standard. A convenient way of displaying the optical absorption spectrum of a material and to define its optical band gap is using Tauc plot. The following relational expression proposed by Tauc is used:[49]

$$(\alpha h\upsilon)^{1/n} = A(h\upsilon - E_g) \quad (3)$$

where h is the Planck's constant, υ is the frequency of vibration, α is the absorption coefficient, E_g is the band gap of the material, n denotes the nature of the electronic transition, for direct transition, $n = 1/2$, and for indirect transition, $n = 2$, and A is the constant.[46] The acquired reflectance data was converted to $F(R_\infty)$ values by the application of the Kubelka–Munk algorithm and the function $F(R_\infty) = (1 - R_\infty)^2/2R_\infty$ is used as the equivalent of absorbance, wherein R_∞ is the diffuse reflectance of an infinitely thick sample layer and $F(R_\infty)$ is usually termed the Kubelka–Munk (K-M) function. Thus, α in the Tauc equation (eq 3) is substituted with $F(R_\infty)$ and the Tauc equation can be rewritten for diffuse reflectance calculations as

$$(F(R_\infty)h\upsilon)^{1/n} = A(h\upsilon - E_g) \quad (4)$$

A curve that plots the value of $h\upsilon$ on the horizontal axis and $(F(R_\infty)h\upsilon)^{1/n}$ on the vertical axis is drawn. The linear extrapolation of $[F(R_\infty)h\upsilon]^{1/n}$ to the abscissa at zero $F(R_\infty)$ permits estimation of the band gap energies of these samples.

N_2 Adsorption–Desorption Isotherms. To determine the Brunauer–Emmett–Teller (BET) surface area of the as-synthesized samples, nitrogen adsorption–desorption measurements were performed at the temperature of liquid nitrogen (~77 K) using a Quanta Chrome (Nova 2000e) surface area analyzer. Prior to N_2 adsorption, the samples (~100 mg) were degassed in vacuum at 70 °C for 8 h to clean the unwanted adsorbants from the surface. The BET surface area was determined by a multipoint BET method using the adsorption data in the relative pressure (P/P_0) range of 0.05–0.30.

Photocatalytic Activity Tests. The photocatalytic performance of the as-synthesized samples was evaluated by observing their abilities to degrade the methylene blue (MB) dye, which is adopted as a representative organic pollutant of dye wastewater, in aqueous solution under simulated visible irradiation induced by a 100 W tungsten lamp equipped with UV cut off filter to remove the radiation below 420 nm. The photocatalytic tests were performed in a reactor equipped with a cooling water cycle system to keep the temperature stable. In a typical visible-light photocatalytic experiment, the catalyst (20 mg) was dispersed in a 50 mL aqueous solution of methylene blue (1×10^{-5} M) and the obtained catalyst suspensions were magnetically stirred at 300 rpm in the dark for 1 h to ensure adsorption/desorption equilibrium between catalyst and organic dye. The catalyst suspension was subsequently irradiated with a 100 W tungsten lamp, placed at a working distance of 10 cm from the light source to initiate the photocatalytic reaction. Adequate aliquots (2 mL) of the suspension were extracted and centrifuged at 10 000 rpm after every 5 min during the course of 60 min irradiation to remove the residual catalyst particulates for analysis. Analogous control experiments were performed either without catalyst or in the dark to attest that the degradation reaction is solely driven by a photocatalytic process. The photodegradation efficiency was monitored by measuring the change in intensity of the characteristic absorbance of MB at 664 nm using Shimadzu UV-2450 spectrometer with 10 mm path length quartz cells. The photodegradation efficiency (D) of each catalyst was computed using the following equation[50]

$$D(\%) = 100 \times (C_0 - C)/C_0 \quad (5)$$

where C is the concentration of MB at the time interval t and C_0 is the concentration after the adsorption equilibrium is reached before irradiation.

Identification of Reactive Species Generated during Photocatalysis. To gain an understanding of the mechanism of photocatalytic degradation of MB over $NaNbO_3$/CdS core/shell heterostructures under visible light irradiation, trapping experiments using active species scavengers were performed. Controlled photoactivity experiments using different active species scavengers were conducted similarly to the above photocatalytic degradation of MB except that active species scavengers (10 mM) were added to the MB solution prior to the addition of the photocatalysts. Ammonium oxalate as scavenger for photogenerated holes (h^+), $AgNO_3$ as the scavenger for electrons (e^-), benzoquinone as the scavenger for superoxide radical anions ($O_2^{\bullet-}$), and *tert*-butanol for hydroxyl radicals ($OH^\bullet$) were introduced to examine the predominant active species participating in the photodegradation of MB over $NaNbO_3$/CdS core/shell heterostructures.

Photoluminescence (PL) Spectra. The photoluminescence (PL) spectra of the as-synthesized samples in the powder form were investigated at room temperature on a Fluoromax-4 fluorescence spectrophotometer (Horiba Jobin Yvon Japan) with an excitation wavelength (λ_{ex}) of 340 nm and the width of the excitation and emission slit were 2 and 5 nm, respectively. The emission spectrum was monitored over a wavelength range of 300–700 nm.

Stability and Reusability of the Photocatalysts. Additionally, the recycling experiments were performed for three consecutive cycles to test the stability and reusability of the photocatalysts. At each cycle interval, the photocatalysts were recycled using a high speed centrifuge and washed thoroughly with water and ethanol several times to remove residual dye impurities, and subsequently dried at 60 °C for the next photocatalytic test. Cycling experiments and X-ray diffraction studies were utilized to access the evaluation of stability and reusability of the core/shell heterostructures.

RESULTS AND DISCUSSION

By suitably modulating the experimental parameters such as cadmium and sulfur precursor concentration as well as by varying the amounts of MPA, a controlled shell thickness of $NaNbO_3$/CdS heterostructures was achieved. The present $NaNbO_3$/CdS core/shell heterostructures are thoroughly characterized by XRD, FESEM, TEM, EDS, and DRS studies and provide an ideal platform to study the photodegradation of organic pollutants such as methylene blue. The results of $NaNbO_3$/CdS core/shell heterostructures obtained with optimized conditions, accompanied by comparison with the individual counterparts ($NaNbO_3$ nanorods: diameter ~100 nm and CdS nanoparticles: diameter 40 nm) are discussed here.

XRD Analysis. Information regarding the phase composition, purity, and crystallinity of the as-synthesized samples were procured by X-ray diffraction (XRD) analysis, and the results

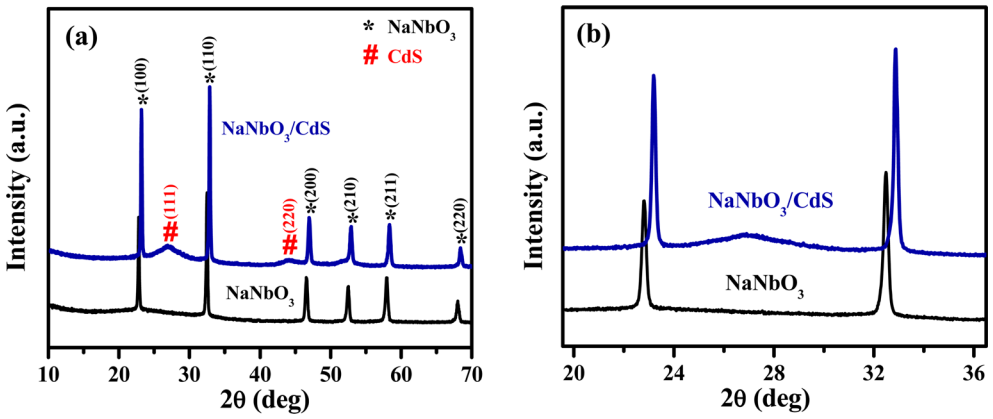

Figure 1. (a) XRD patterns of $NaNbO_3$ nanorods and $NaNbO_3$/CdS core/shell heterostructures, and (b) XRD patterns of $NaNbO_3$ nanorods and $NaNbO_3$/CdS core/shell heterostructures showing shift in the peak position due to core/shell formation.

obtained are shown in Figure 1. Qualitative analysis of the XRD patterns (shown in Figure 1a) indicates that all the diffraction peaks of $NaNbO_3$ correlate closely with the documented orthorhombic phase of $NaNbO_3$ (JCPDS card no. 895173), with some additional peaks at 2θ values of 26.90° and 43.84° are undisputedly indexed to (111) and (220) crystallographic planes of cubic CdS (JCPDS card no. 751546), respectively. An interesting finding scrutinized from the XRD patterns is that the diffraction peaks corresponding to $NaNbO_3$ in $NaNbO_3$/CdS core/shell heterostructures shifts toward a higher 2θ values (Figure 1b). Based on Bragg's law,[51] the observed shift of the diffraction peaks to larger angle directly reflects the lattice shrinkage of the $NaNbO_3$ with the growth of CdS shell and implies the existence of strain between the core and shell material. Evidence of strain in these core/shell heterostructures is supported from the Williamson-Hall (W−H) plot using the following equation[47]

$$\beta \cos \theta/\lambda = 1/D + \eta \sin \theta/\lambda \quad (1)$$

where β is the full width at half-maximum (fwhm) of $\theta - 2\theta$ peak, θ is the diffraction angle, λ is the X-ray wavelength, η is the effective strain, and D is the crystallite size. The strain (η) is calculated from the slope and the crystallite size (D_{WH}) is calculated from the intercept of the plot of $\beta \cos \theta/\lambda$ against sin θ/λ. Consideration of slope of the fitted line in W−H plots shown in Figure 2 would lead to a conclusion that the bare

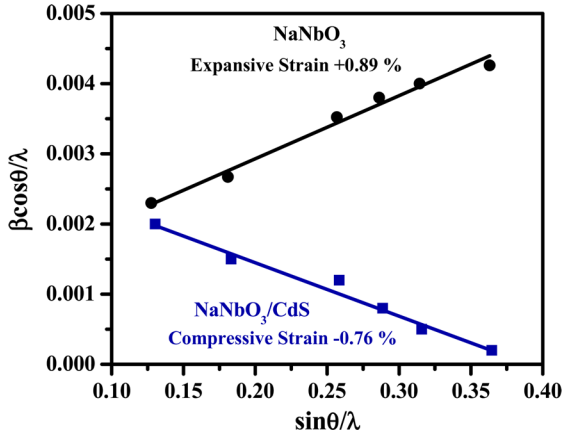

Figure 2. Williamson-Hall plot for $NaNbO_3$ nanorods and $NaNbO_3$/CdS core/shell heterostructures.

$NaNbO_3$ experiences a net expansive strain (positive strain, +0.0089), while as the shell is grown, $NaNbO_3$ experiences a net compressive strain (negative strain, −0.0076). The expansive strain in $NaNbO_3$ nanorods developed itself during the preparation method.[52] The negative strain existing in $NaNbO_3$ is the consequence of the CdS shell which compresses the lattice planes of $NaNbO_3$ and shifts the diffraction peaks toward larger angle.[53] The crystallite size that takes strain into account can be estimated from the intercept of the fitted line shown in Figure 2. Concerning the crystallite sizes, a calculation based on both Williamson−Hall plot (D_{WH}) and Scherrer formula (D_{Sch}) are consistent with each other. The calculated lattice paramters, D_{Sch}, η, and D_{WH} values have been summarized in Table 1. Thus, XRD investigations conclude the existence of orthorhombic $NaNbO_3$ along with the cubic CdS in $NaNbO_3$/CdS heterostructures and also hints at the possibility of formation of core/shell morphology between $NaNbO_3$ and CdS through Williamson-Hall analysis; however, the confirmation of core/shell morphology is substantiated by additional results as discussed below.

Raman Studies. Raman spectroscopy, a more surface sensitive technique, was utilized as an additional tool to probe the phase composition in core/shell heterostructures. As follows in Figure 3, Raman measurements of $NaNbO_3$/CdS core/shell heterostructures, $NaNbO_3$ nanorods, and CdS nanoparticles were probed. Our Raman characterization of $NaNbO_3$ and CdS is in accord with the previous work[54,55] indicating the defect-free synthesis of $NaNbO_3$ nanorods, which were utilized in the synthesis of core/shell heterostructures. Interestingly, subsequent to the growth of CdS shell onto $NaNbO_3$, the core/shell heterostructures manifest the Raman features of $NaNbO_3$ and CdS. However, the intensity of Raman band at 600 cm^{-1} is remarkably enhanced and the peak is broadened owing to the overlap of Raman band of $NaNbO_3$ with CdS. The observed mode wavenumbers and proposed assignments are summarized in Table 2. Thus, the results acquired through Raman measurements show the existence of $NaNbO_3$ and CdS in the core/shell heterostructures and support the XRD results.

FESEM Analysis. To probe the surface morphology of $NaNbO_3$ before and after growth of CdS shell, we performed the field-emission scanning electron microscopy (FESEM) measurements. Apparently, the initial $NaNbO_3$ has uniform rod-like morphology manifesting an average length of 1 ± 0.02 μm and uniform diameter in the range of 100 ± 5 nm along the

Table 1. Crystallite Size, Cell Parameters, and Lattice Strain of $NaNbO_3$ and $NaNbO_3$/CdS Core/Shell Heterostructures

sample	shell thickness (nm)	crystallite size (Scherrer equation) D_{Sch} (nm)	crystallite size (Williamson and Hall method) D_{WH} (nm)	cell parameter (Å)	lattice strain (%)
$NaNbO_3$	-	49.7	49.3	a = 5.502 (6) b = 5.562 (3) c = 15.518 (5)	+0.89
$NaNbO_3$/CdS	40	44.4	44.2	a = 5.498 (4) b = 5.557 (6) c = 15.514 (1)	−0.76

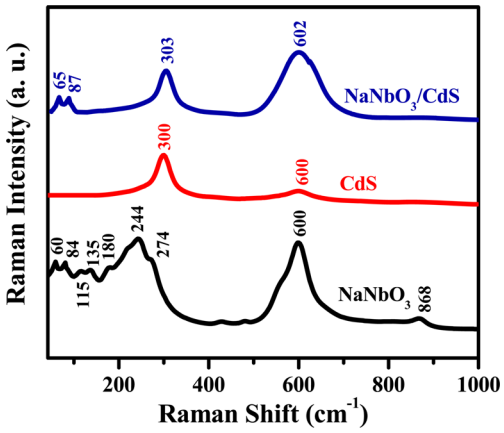

Figure 3. Raman Spectra of $NaNbO_3$/CdS core/shell heterostructures, $NaNbO_3$ nanorods, and CdS nanoparticles.

Table 2. Observed Wavenumbers of $NaNbO_3$, CdS, and $NaNbO_3$/CdS Core/Shell Heterostructures in the Raman Spectra

$NaNbO_3$ (cm^{-1})	CdS (cm^{-1})	$NaNbO_3$/CdS (cm^{-1})
60, 84 (translational modes involving Na^+ cation motion against NbO_6 octahedra)	300 (first-order longitudinal optical phonon)	65, 87 (from $NaNbO_3$)
115, 135 (NbO_6 libration)	600 (second-order longitudinal optical phonon)	303 (from CdS)
180, 244, 274, 600, 868 (internal modes of NbO_6 ions)	-	602 (from $NaNbO_3$ and CdS)

entire length with smooth surfaces, as shown in Figure 4a. Following the addition of Cd and S precursors, it is discerned from Figure 4b that the overall alignment of the nanorods is still preserved. However, compared to $NaNbO_3$ nanorods, the $NaNbO_3$/CdS heterostructures exhibit a larger diameter and rougher surface, indicating the successful deposition of CdS outlayer on $NaNbO_3$ nanorods.

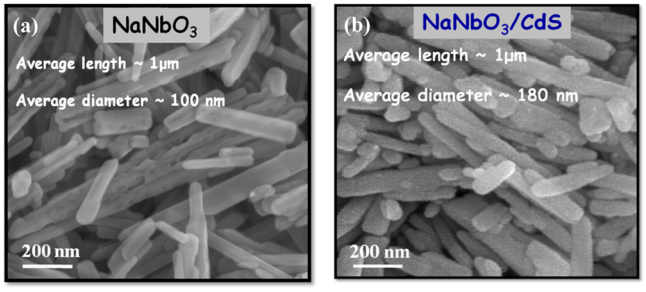

Figure 4. FESEM images of (a) $NaNbO_3$ nanorods and (b) $NaNbO_3$/CdS core/shell heterostructures.

FESEM-EDS Elemental Mapping Analysis. To unravel the elemental composition and the amount of distribution of elements present in $NaNbO_3$/CdS core/shell heterostructures, energy dispersive X-ray spectroscopy (EDS) elemental mapping was conducted. The mapping results (Figure 5b–f) of the selected rectangular area of FESEM image of a single $NaNbO_3$/CdS core/shell nanorod (Figure 5a) clearly depicted the coexistence of Na, Nb, O, Cd, and S elements in the heterostructures. Noticeably, the distribution of all the elements is homogeneous and uniform, however, the distribution of Cd and S elements exhibits a much larger area than the other elements,[56] endorsing that $NaNbO_3$ nanorod cores are densely and uniformly encased by CdS nanoparticles and results in formation of core/shell heterostructures.

TEM Analysis. Convincing proof of the core/shell formation in $NaNbO_3$/CdS heterostructures is revealed by TEM and HRTEM studies. Analysis of the TEM results manifested in Figure 6a shows $NaNbO_3$ core nanorod with a diameter of ∼100 nm and the surrounding CdS shell with an average thickness of ∼40 nm. The brightness difference between the core and the shell in the magnified TEM image portrayed in the inset of Figure 6a clearly substantiates the existence of a core/shell configuration of the heterostructures. Shown in Figure 6b is a HRTEM image of the $NaNbO_3$/CdS core/shell heterostructures. By analyzing the interface of the core and the shell in HRTEM taken from the selected rectangular region of $NaNbO_3$/CdS heterostructures (as marked in Figure 6a), we observe that the lattice fringes are continuous from the core to the shell. Due to the thickness, the lattice fringes of $NaNbO_3$ core are not observed and only one set of lattice fringes of 0.33 nm corresponding to (111) planes of CdS is discerned in the core and the shell region, which is accredited to the thick shell.[57] Thus, TEM and HRTEM analysis explicitly validates the core/shell morphology of $NaNbO_3$/CdS heterostructures.

Synthesis of the CdS nanoparticles (of average size 40 nm) is supported from the TEM results as displayed in Supporting Information Figure S1.

TEM Point EDS Analysis. Additional support for the core being made up of $NaNbO_3$ and the shell consisting of CdS was finally provided by point-EDS. Figure 7 displays a comparison of point-EDS acquired by positioning the electron beam through the center (core/shell) and only through edge (shell). The copper and carbon signals came from the TEM grid. It can be vividly seen from Figure 7 that on positioning the electron probe through the center of the material and focusing on the core, unveiled significantly intense signals of Na, Nb, and O and weaker signal of Cd and S elements while stronger Cd and S signals are detected in the shell region, accompanied by weaker signal of Na, Nb, and O elements, which unambiguously

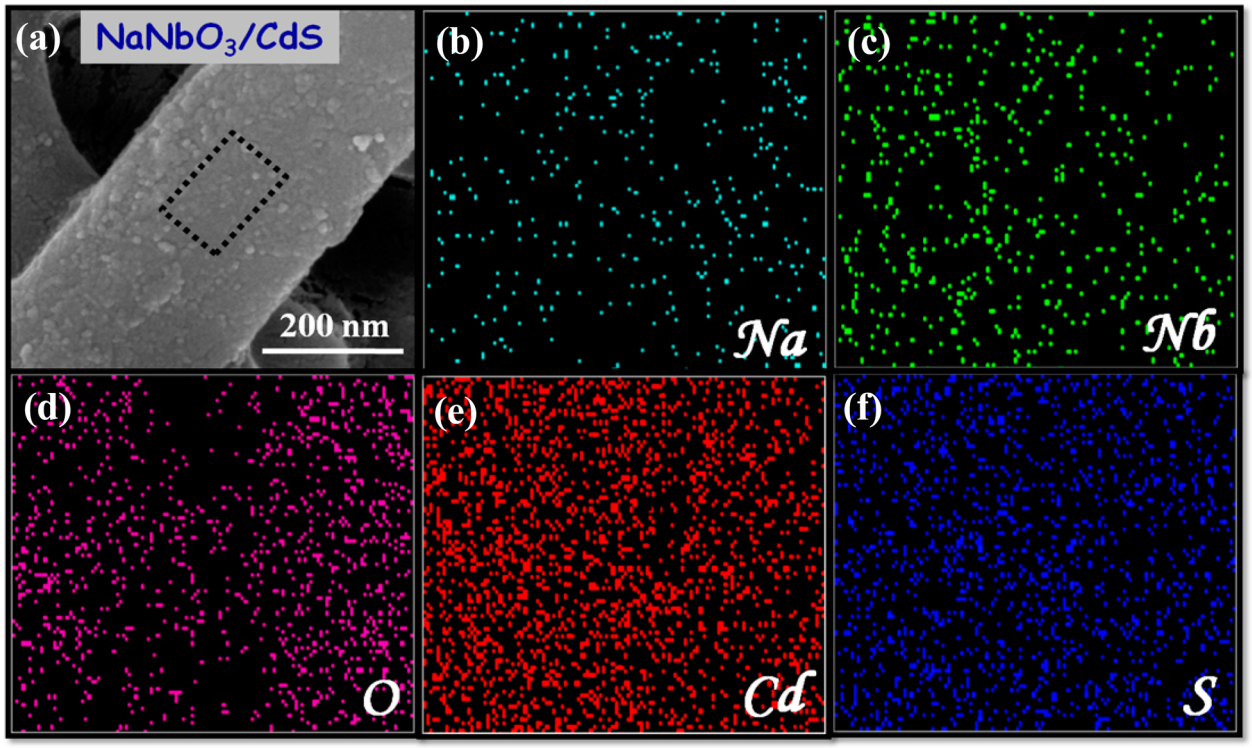

Figure 5. (a) Magnified FESEM image of single $NaNbO_3$/CdS core/shell nanorod, and EDS mapping of (b) Na, (c) Nb, (d) O, (e) Cd, and (f) S element in $NaNbO_3$/CdS core/shell nanorod.

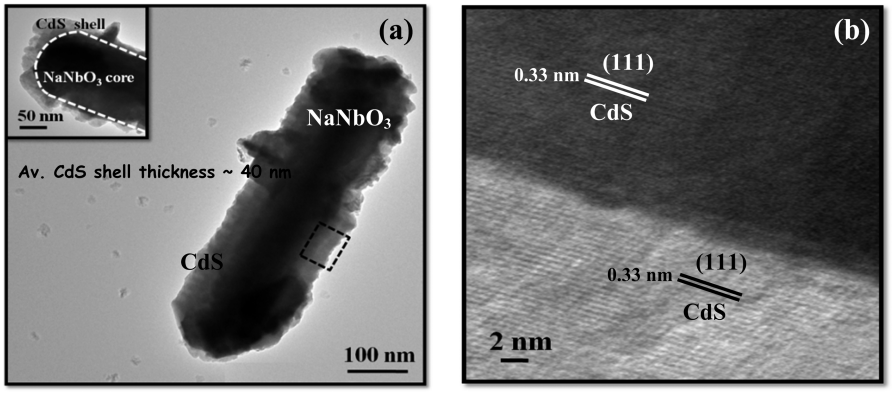

Figure 6. (a) TEM image and (b) HRTEM image of $NaNbO_3$/CdS core/shell heterostructures. The inset in (a) shows the magnified TEM image of $NaNbO_3$/CdS core/shell heterostructures.

confirms the core/shell configuration of the as-synthesized $NaNbO_3$/CdS heterostructures. Thus, combinatorial techniques of FESEM, FESEM-EDS elemental mapping, TEM, HRTEM, and point-EDS analysis make it possible to unanimously conclude the core/shell morphology of $NaNbO_3$/CdS heterostructures.

UV–vis DRS Analysis. The light absorption properties of the as-synthesized samples were analyzed by UV–vis diffuse reflectance spectroscopy (UV–vis DRS). Figure 8 portrays the UV–vis diffuse reflectance spectra of $NaNbO_3$, CdS, and $NaNbO_3$/CdS core/shell heterostructures. As expected, $NaNbO_3$ nanorods exhibit a pronounced absorption band in the UV region at 371 nm, which is ascribed to electron promotion from the valence band to conduction band.[58] Integrating CdS onto $NaNbO_3$ nanorods results in considerable red shift in the absorption onset of $NaNbO_3$ which is implicit of the interfacial interaction between the $NaNbO_3$ nanorods and CdS shell.[59] This revolution is easily discernible from the color change from white to yellow as shown in the inset of Figure 8a, and can be underpinned by the band gap estimation using the Kubelka–Munk equation. Assuming the core/shell catalysts to be direct semiconductors, like $NaNbO_3$ and CdS (as a reasonable linear behavior is observed for $NaNbO_3$ and CdS with exponent 1/2, corresponding to direct transition), a plot of the modified Kubelka–Munk function versus the energy of photon energy (as reflected in Figure 8b) affords band gap energies of 3.35, 2.95, and 2.60 eV for $NaNbO_3$, $NaNbO_3$/CdS, and CdS, respectively. To sum up, the DRS result mirrors substantial visible light photoactivity of $NaNbO_3$/CdS core/shell heterostructures, and therefore, core/shell heterostructures are expected to possess visible-light driven photocatalytic abilities.

BET Surface Area Analysis. Before moving toward the photocatalytic study of the as-synthesized samples, analysis of

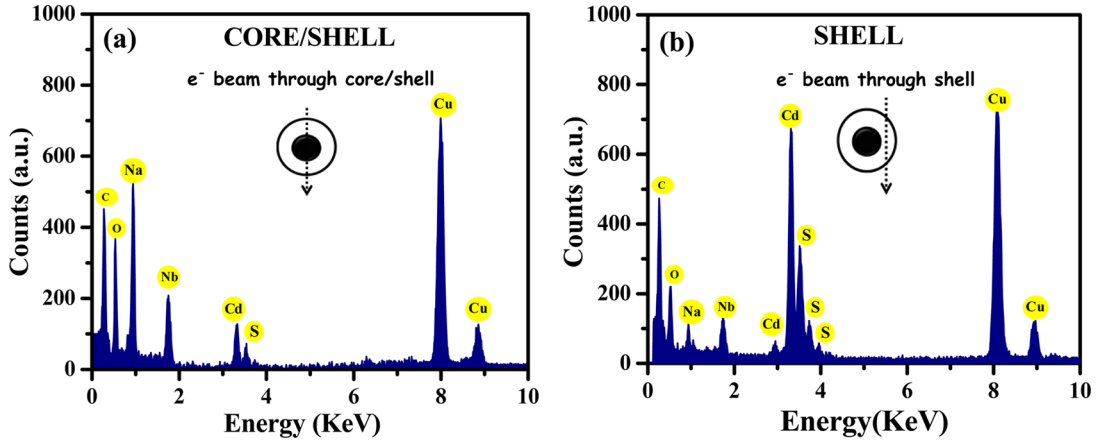

Figure 7. EDS analysis of the marked region in Figure 5a corresponding to (a) core/shell and (b) shell of $NaNbO_3$/CdS heterostructures.

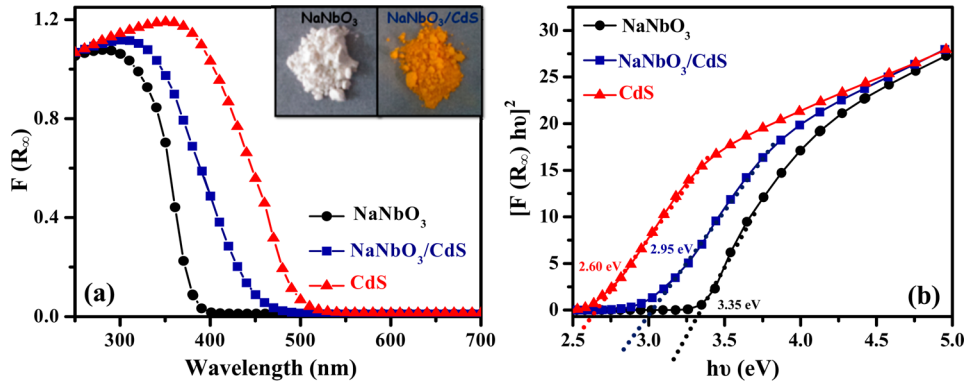

Figure 8. (a) UV–vis DRS of $NaNbO_3$, CdS, and $NaNbO_3$/CdS core/shell heterostructures, and (b) Kubelka–Munk plot for band gap calculation of $NaNbO_3$, CdS, and $NaNbO_3$/CdS core/shell. The inset in (a) shows the snapshots of $NaNbO_3$ and $NaNbO_3$/CdS core/shell heterostructures samples.

surface area, a vital factor influencing the photocatalysis, is indispensable. In general, a larger surface area can render more adsorption and reaction sites for photocatalytic reactions and improved transport of charge carriers, leading to an enhancement in the rate of degradation of organic pollutants.[60] To ascertain the surface area of the as-synthesized samples, nitrogen adsorption–desorption isotherms are measured. The Brunauer–Emmett–Teller (BET) surface area measurements give a surface area value of about 7.18, 9.61, and 77.03 $m^2\ g^{-1}$ for the $NaNbO_3$ nanorods, CdS nanoparticles, and $NaNbO_3$/CdS core/shell heterostructures, respectively. The results of BET surface area analysis (as displayed in Figure 9 and Supporting Information Figure S2) revealed that the growth of CdS shell onto the $NaNbO_3$ nanorods greatly enhances the surface area of the resulting core/shell heterostructures. The enhanced surface area stemming from the rough surface of core/shell heterostructures could facilitate more surface active sites, and thus we anticipate that these $NaNbO_3$/CdS core/shell heterostructures are conducive to enhancing the photocatalytic performance.

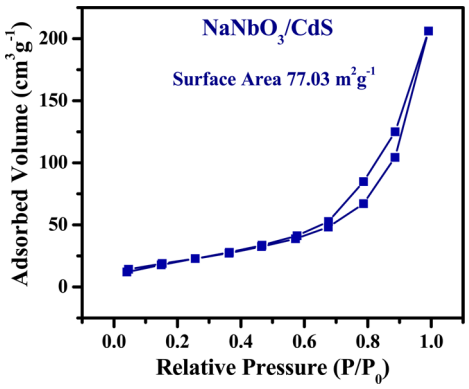

Figure 9. Nitrogen adsorption–desorption isotherms of the $NaNbO_3$/CdS core/shell heterostructures.

Visible-Light-Driven Photocatalytic Activity. Dyes are pervasive commercial chemicals that manifest unique environmental problems.[61,62] The largest discharge of dyes into the environment occurs via the dye effluents from textile mills and confers an acute problem for municipal waste treatment facilities. Quite apart from the aesthetic desirability of colored streams resulting from dye waste, these dyes can undergo natural anaerobic degradation to potentially carcinogenic amines. Treatment of dye-based effluents is considered to be one of the more challenging tasks in environmental fraternity. Technologies involving physical or biological treatments[63,64] do not achieve significant organic dye pollutant degradation. However, semiconductor photocatalysis, an alternative treatment strategy can successfully oxidize notorious organic dye pollutants existing in wastewater. Thus, to investigate the merits of $NaNbO_3$/CdS core/shell heterostructure photocatalyst under visible light irradiation, we have utilized methylene blue (MB) dye as a target pollutant of dye wastewater. The characteristic absorption peak of MB at 664 nm was pursued to

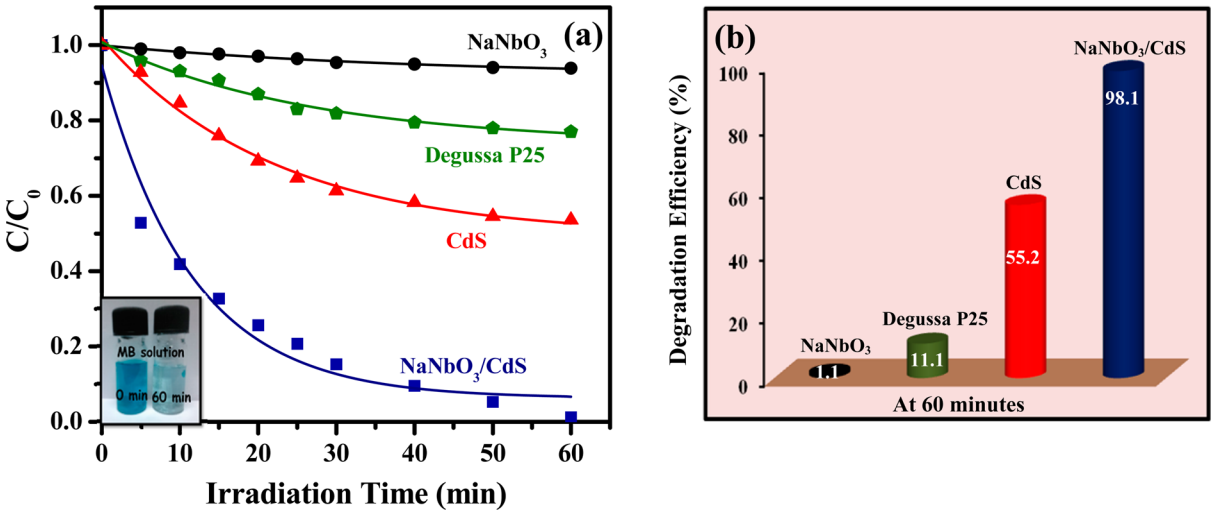

Figure 10. (a) Photocatalytic performance and (b) degradation efficiency of $NaNbO_3$ nanorods, CdS nanoparticles, Degussa P25, and $NaNbO_3$/CdS core/shell heterostructures for the degradation of MB solution under visible light irradiation.

monitor the photocatalytic degradation process at different time intervals of visible-light exposure. Blank experiments (i.e., without catalyst or visible light; not shown here) evince negligible photocatalytic activities, thus corroborating that the degradation reaction are truly driven by a photocatalytic process. As evident from Figure 10 and color contrast of the MB dye solution after 60 min (as shown in the inset of Figure 10a), the photocatalytic performance of $NaNbO_3$/CdS core/shell heterostructures to degrade MB under visible light irradiation surpasses that of its individual counterparts. The photodegradation efficiency curve disclosed in Figure 10b unveiled that the MB was almost degraded after 60 min in the presence of core/shell heterostructures, whereas ~99% and 45% of the MB remained in the presence of $NaNbO_3$ nanorods and CdS nanoparticles, respectively.

The photocatalytic decomposition of organic pollutants in water generally follows the Langmuir–Hinshelwood mechanism[65]

$$r = \frac{kKC}{1 + KC} \tag{6}$$

where r is the photocatalytic reaction rate (mol L^{-1} min^{-1}), k is the photocatalysis rate constant (mol L^{-1} min^{-1}), K is the equilibrium adsorption coefficient (L mol^{-1}), and C is the reactant concentration (mol L^{-1}) at time t. At low substrate concentrations, the term KC (eq 6) in the denominator can be neglected with respect to unity and the reaction kinetics exhibit first-order behavior, i.e., $r = kKC$. This kinetic equation may be written in the integral form

$$\ln \frac{C_0}{C} = kKt = k_{app}t \tag{7}$$

where C_0 is the initial reactant concentration (mol L^{-1}) and k_{app} is the apparent photocatalysis rate constant (min^{-1}) of the pseudo-first-order reaction. To make a more convenient comparison, the reaction kinetics of core/shell heterostructures and its individual counterparts were fit into a pseudo-first-order model. Calculations showed that the logarithmic plots of MB concentration versus time for $NaNbO_3$/CdS core/shell heterostrcutures were approximately linear, indicating that the overall catalytic kinetic of MB degradation accord with a first-order reaction. However, ultimate validation of our premise that $NaNbO_3$/CdS core/shell heterostructures are efficient photocatalysts requires comparative investigation with photocatalytic standard, commercial TiO_2 (Degussa P25). As noted from Figure 10, Degussa P25 showed relatively poor photocatalytic activity due to its limited photoresponding range and only 11% of the MB was diminished in 60 min which could be rationalized with high surface area of the P25 sample. The apparent rate constants calculated from the slope of the linear plots of $\ln(C_0/C)$ versus irradiation time t illustrated in Figure 11 were utilized to compare the photocatalytic activities of the

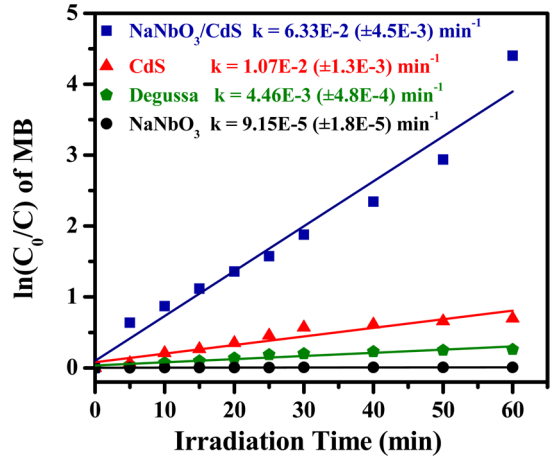

Figure 11. Plot of $\ln(C_0/C)$ as a function of visible irradiation time for photocatalysis of MB solution containing: $NaNbO_3$ nanorods, CdS nanoparticles, Degussa P25, and $NaNbO_3$/CdS core/shell heterostructures under visible light irradiation.

as-synthesized samples are summarized in Table 3. The best apparent degradation rate constant (6.33×10^{-2} ($\pm 4.5 \times 10^{-3}$)), which was higher than that of pure $NaNbO_3$ and Degussa P25 by a factor of 692 and 14, respectively, was obtained for $NaNbO_3$/CdS core/shell heterostructures. Thus, unquestionably, $NaNbO_3$/CdS core/shell heterostructures display impressive photocatalytic activity under visible light irradiation toward MB degradation relative to pure $NaNbO_3$ and benchmark material Degussa P25. Now, it is important to clarify the intrinsic root causes of the enhanced photocatalytic

Table 3. Optical Properties, Photocatalytic Acitivities, and Surface Area of $NaNbO_3$, CdS, and $NaNbO_3$/CdS Core/Shell Heterostructures

sample	shell thickness (nm)	band gap (eV)	surface area (m^2 g^{-1})	photocatalytic efficiency (%)	rate constant (min^{-1})
$NaNbO_3$	-	3.35	7.18	1.1	9.15×10^{-5} ($\pm$ 1.8×10^{-5})
CdS	-	2.60	9.61	55.2	1.07×10^{-2} ($\pm$ 1.3×10^{-3})
$NaNbO_3$/CdS	40	2.95	77.03	98.1	6.33×10^{-2} ($\pm$ 4.5×10^{-3})

ability of the $NaNbO_3$/CdS core/shell heterostructures. We credit this markedly enhanced photocatalytic efficiency to the following three factors:

1. Enhanced Adsorption. One of the factors accounting for the remarkably enhanced photocatalytic efficiency of core/shell heterostructures is the enhanced adsorption of dye molecules, which results from the high surface areas of heterostructures. The large surface area renders more surface active sites and offers more opportunity for the diffusion and mass transportation of MB dye molecules, leading to significantly enhanced photocatalytic efficiency of core/shell heterostructures compared to its individual counterparts.

2. Expanded Visible Light Absorption. Another origin for the outstanding photocatalytic performance of core/shell heterostructures is the expanded visible light absorption. As mirrored in DRS studies (Figure 8) that integrating CdS onto $NaNbO_3$ nanorods results in an extended photoresponse range of approximately 370 to 420 nm (corresponding to visible region of electromagnetic spectrum) and a noticeable reduction of band gap energy, implying a high potential for the utilization of solar light and thus imparting superior photocatalytic activity to the core/shell heterostructures.

3. Efficient Separation of Photogenerated Carriers. The third and most crucial factor encouraging the significantly enhanced photocatalytic performance of core/shell heterostructures is the facile transportation and separation of photogenerated charge carriers. This efficient separation of charge carriers in core/shell heterostructures could be explained by "staggered type-II configuration" formed at the core/shell interface of $NaNbO_3$/CdS heterostructures. The proposed type-II band alignment in $NaNbO_3$/CdS core/shell heterostructures is ideal for photocatalytic applications where charge separation is desirable. To explain the type-II band alignment, the relative band edge positions of the two semiconductors are investigated using the following empirical formula[66]

$$E_{CB} = X + E_0 - 0.5E_g \quad (8)$$

and

$$E_{VB} = E_{CB} + E_g$$

where E_g refers to the band gap energy of the semiconductor, E_{CB} is the conduction band potential, E_{VB} is the valence band potential, E_0 is scale factor relating the reference electrode redox level to the absolute vacuum scale (E_0 = −4.5 eV for normal hydrogen electrode), and X is the electronegativity of the semiconductor, which can be expressed as the geometric mean of the absolute electronegativity of the constituent atoms. Following the above equation, the calculated values of CB and VB potential of $NaNbO_3$ and CdS are summarized in Table 4.

Table 4. Calculated Values of Conduction Band (CB) and Valence Band (VB) Positions of $NaNbO_3$, CdS, and $NaNbO_3$/CdS Core/Shell Heterostructures

sample	shell thickness (nm)	band gap (eV)	conduction band (eV)	valence band (eV)
$NaNbO_3$	-	3.35	−0.60	2.75
CdS	-	2.60	−0.70	1.90
$NaNbO_3$/CdS	40	2.95	−0.60 ($NaNbO_3$)	2.75 ($NaNbO_3$)
			−0.70 (CdS)	1.90 (CdS)

From the obtained values, it is evident that the CB and VB potential of CdS is at higher potential than that of $NaNbO_3$ correlating with the type-II band alignment, in which both the conduction and valence bands of shell are either lower or higher than those in the core. The type-II band alignment in $NaNbO_3$/CdS core/shell heterostructures is delineated in Figure 12. From the band alignment diagram of core/shell

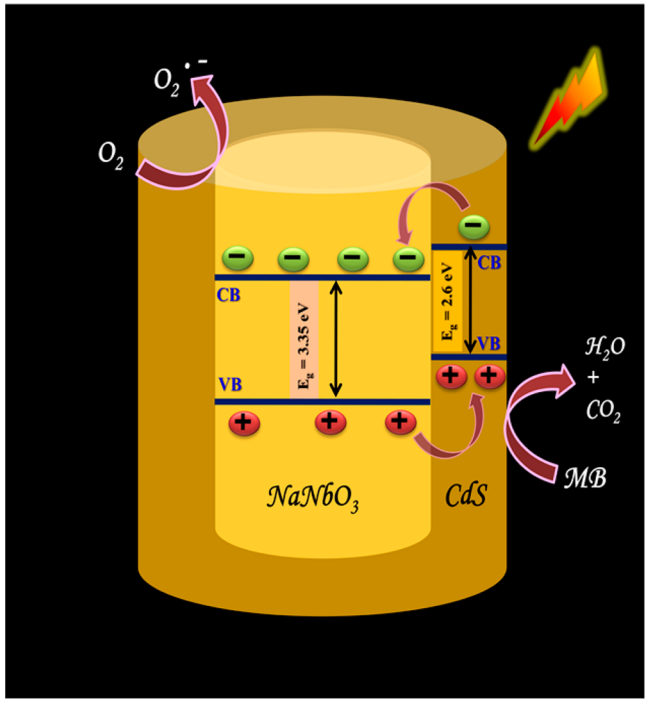

Figure 12. Schematic diagram showing separation of photogenerated charge carriers in $NaNbO_3$/CdS core/shell heterostructures.

heterostructures it is discerned that when CdS is irradiated by photon energy surpassing its band gap energy, electrons are photoexcited from the VB to the CB leaving holes in the VB and then electron transfer from the CB of CdS to the CB of the $NaNbO_3$ driven by the decreased potential energy, and conversely, holes transfer from the VB of $NaNbO_3$ to the VB of CdS under visible light irradiation. Consequently, the photogenerated electrons and holes were separated at the $NaNbO_3$/CdS core/shell interfaces, which reduced their recombination probability and authorized them to migrate effectively to the surfaces of $NaNbO_3$ and CdS. These photogenerated charge carriers immediately join in the redox

reactions and result in the formation of active species, which participate in the degradation of MB. Organic dye pollutants (MB) are eventually oxidized by these highly active species to stable inorganic compounds. Thus, the above factors involving extended light absorption, core/shell morphology, and high surface areas taken together result in remarkably enhanced photocatalytic activity of $NaNbO_3$/CdS core/shell heterostructures.

Mechanism of Photocatalysis. Subsequent to identifying the band alignment in $NaNbO_3$/CdS core/shell heterostructures, it is imperative to understand the mechanism of photocatalysis of MB under visible light irradiation. To unfold the mechanism of photodegradation of MB using $NaNbO_3$/CdS core/shell heterostructure photocatalyst, a series of quenchers were employed to ascertain the ruling active species. Benzoquinone (BQ) as a scavenger for $O_2^{\bullet-}$, ammonium oxalate (AQ) for h^+, $AgNO_3$ for e^-, and *t*-BuOH for $OH^\bullet$ were introduced to the MB solution prior to the addition of core/shell photocatalyst.[67] As an outcome of quenching, the more photocatalytic efficiency is reduced by the scavengers, the more pivotal the corresponding oxidizing species is in the photodegradation. Presented in Figure 13 is the photodegradation of

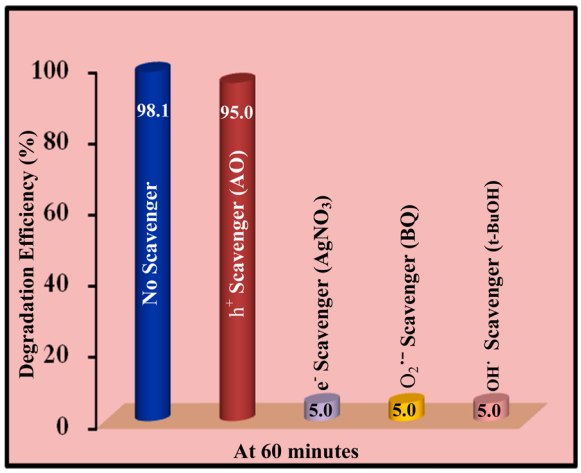

Figure 13. Effects of a series of scavengers on the photodegradation efficiency of MB using $NaNbO_3$/CdS core/shell heterostructures.

MB over $NaNbO_3$/CdS core/shell heterostructure photocatalyst in the presence of active species scavengers. The addition of $AgNO_3$ (electrons scavenger) and BQ (superoxide radical anions scavenger) substantially reduced the photodegradation of MB. A similar inhibition phenomenon is observed with the introduction of *t*-butanol (hydroxyl radicals scavenger) on the photodegradation of MB. However, the addition of AO (holes scavenger) only caused a small decrease in the photocatalysis of MB.

Directed by the above findings from the active species trapping experimental results, we concluded that $OH^\bullet$, ensuing through the involvement of photogenerated electrons and superoxide radical anions, is the predominant contributor to the photocatalysis of MB over $NaNbO_3$/CdS core/shell heterostructures and that photogenerated holes play an assistant role. On the basis of the above conclusion, we propose below a plausible mechanism for the photodegradation of MB over $NaNbO_3$/CdS core/shell heterostructures.

$$CdS + h\nu \rightarrow CdS(e^-_{CB}.....h^+_{VB})$$

$$CdS(e^-_{CB}) + NaNbO_3 \rightarrow CdS + NaNbO_3(e^-_{CB})$$

$$NaNbO_3(e^-_{CB}) + O_2 \rightarrow NaNbO_3 + O_2^{\bullet-}$$

$$O_2^{\bullet-} + H_2O \rightarrow HO_2^\bullet + OH^-$$

$$HO_2^\bullet + H_2O \rightarrow OH^\bullet + H_2O_2$$

$$H_2O_2 \rightarrow 2OH^\bullet$$

$$OH^\bullet + MB \rightarrow CO_2 + H_2O$$

$$CdS(h^+_{VB}) + MB \rightarrow \text{Degraded products}$$

where e^-_{CB} and h^+_{VB} stand for the electron in the conduction band and hole in the valence band, respectively.

Under the irradiation of visible light, the electrons are excited from the valence band (VB) of CdS in $NaNbO_3$/CdS core/shell heterostructures to its conduction band (CB), thereby forming the photoactive species, electron and hole. Simultaneously, the photogenerated electrons can fleetly transfer to the CB of $NaNbO_3$ driven by the decreased potential energy which can be further trapped by molecular oxygen in the reaction system to activate molecular oxygen (e.g., the formation of superoxide radical anion), thus efficiently inhibiting the recombination of electron−hole pairs and prolonging the lifetime of charge carriers. The formed superoxide radical anion sequentially results in the generation of hydroxyl radicals, which are found to be the ruling active species in the photodegradation of MB. The photogenerated holes are also involved in the degradation of MB to some extent as evidenced by the active species trapping experiments. Thus, combining the effect of hydroxyl radicals and photogenerated holes results in degradation of MB over $NaNbO_3$/CdS core/shell heterostructure photocatalyst under visible light illumination.

PL Analysis. The prolonged lifetime and lower recombination rate of photogenerated charge carriers in $NaNbO_3$/CdS core/shell heterostructures could be corroborated by photoluminescence (PL) analysis. Considering that PL emission signals result from the recombination of free carriers, we have employed photoluminescence studies to understand the fate of photogenerated charge carriers. As portrayed in Figure 14, the emission peak in bare CdS and $NaNbO_3$ at 505 and 387 nm is assigned to the band gap transition correlating well to the band gap energy of CdS and $NaNbO_3$, respectively. However, after the growth of CdS shell onto $NaNbO_3$ nanorods, almost

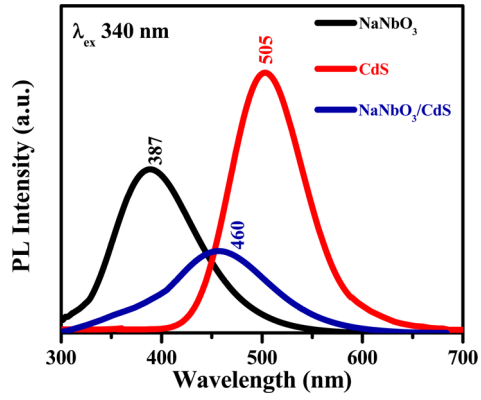

Figure 14. Photoluminescence (PL) spectra of the $NaNbO_3$/CdS core/shell heterostructures, $NaNbO_3$ nanorods, and CdS nanoparticles.

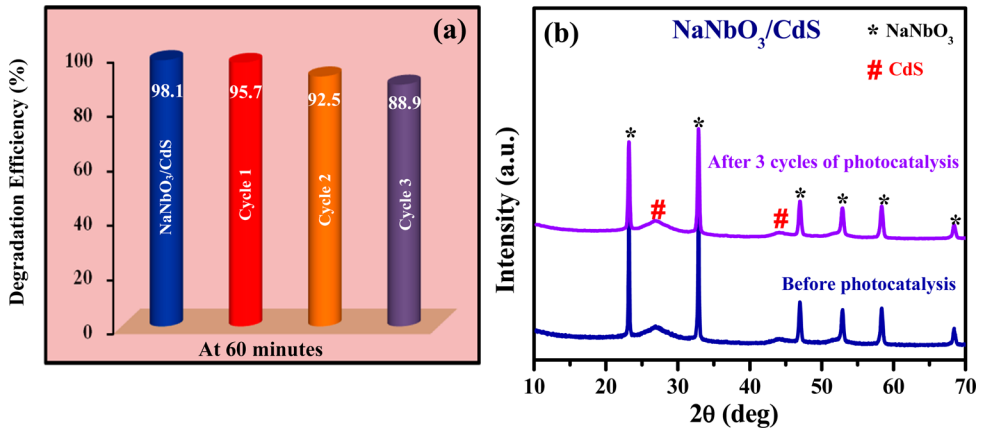

Figure 15. (a) Percent degradation efficiency of $NaNbO_3$/CdS core/shell heterostructures with increasing number of catalytic cycles, and (b) XRD patterns of $NaNbO_3$/CdS core/shell heterostructures before and after photocatalytic reaction.

immediate quenching of the emission of $NaNbO_3$ is observed and a new emission peak at 460 nm appears. The significant shift to the longer wavelengths in the absorption and emission spectra also substantiates the growth of the shell. In addition, the PL intensity of $NaNbO_3$/CdS core/shell heterostructures shows a pronounced decrease compared to the $NaNbO_3$ and CdS, accredited to efficient separation of photogenerated charge carriers driven by the type-II band alignment between $NaNbO_3$ and CdS. As evident from the band diagram of $NaNbO_3$/CdS core/shell heterostructures, both the valence and conduction band of CdS lie above that of $NaNbO_3$, thus forming a staggered type-II band alignment, which allows the transfer of photogenerated electrons from the conduction band of CdS to the conduction band of $NaNbO_3$ and conversely, holes transfer from the valence band of $NaNbO_3$ to the valence band of CdS, under visible light irradiation. As a result, the electrons accumulate in the conduction band of $NaNbO_3$ nanorods and the holes gather in the valence band of CdS, thereby resulting in efficient suppression in recombination of charge carriers and longer lifetime of carriers. Thus, the results drawn from the PL analysis support the fact that the growth of CdS shell onto $NaNbO_3$ could efficiently slow down the recombination of photogenerated carriers and prolong the lifetime of carriers, and thus are accountable for the superior visible light driven photocatalytic activity of the resulting $NaNbO_3$/CdS core/shell heterostructures.

Stability and Reusability of $NaNbO_3$/CdS Core/Shell Heterostructures. The possibility of catalyst reuse and stability in photocatalytic processes is of paramount importance since it could contribute significantly to lowering the operational cost of the process, thus making photocatalysis a captivating approach for dye wastewater treatment. To this end, three consecutive cyclic photodegradation experiments were performed for core/shell heterostructures, each time using the same catalyst and a fresh dye solution. Cycling experiments and X-ray diffraction studies were utilized to access the evaluation of stability and reusability of the core/shell heterostructures. The results of the cycling experiments of the $NaNbO_3$/CdS core/shell heterostructures for photodegradation of MB under visible-light irradiation are depicted in Figure 15a and indicate a trivial decline (~10%) in photocatalytic activity after three cycles, which could originate from the unavoidable loss of the sample during recycling. The photostability of the catalysts was monitored by using X-ray diffraction and TEM studies during the course of photocatalytic reactions and the results in Figure 15b and Supporting Information Figure S3 showed that the recovered catalysts after three photodegradation cycles reveal intact phase of the $NaNbO_3$ and CdS, and no discernible change in morphology, implying that the core/shell heterostructure photocatalyst maintains its structural integrity even after three photocatalysis reactions. Thus, analysis of cycling experiment results reflects the stability and viable potential of the synthesized core/shell heterostructures for practical use in environmental applications.

Thus, the results of this study suggest strongly that control of morphological design and appropriate band alignment allows achievement of highly efficient and reusable visible-light photocatalysts. Further, our results offer broad implications for steering the design and development of novel core/shell heterostructures for wastewater treatment, air purification, and separation technology, among others.

CONCLUSIONS

This work represents the comprehensive study of novel type-II $NaNbO_3$/CdS core/shell heterostructures synthesized by adopting a simple wet chemical approach. Collectively, all of our acquired data, including PXRD, FESEM, TEM, EDS, DRS, and Raman studies, unambiguously support the existence of the reported core/shell heterostructures. We have explored the possibility of photocatalysis in these core/shell heterostructures and found that $NaNbO_3$/CdS core/shell heterostructures manifested superior photocatalytic activity toward methylene blue (MB) degradation under visible light irradiation compared to its counterparts and photocatalytic reference, Degussa P25. It turns out that the core/shell morphology and type-II band alignment resulting from the judicious combination of $NaNbO_3$ and CdS are responsible for the onset of photocatalysis in $NaNbO_3$/CdS core/shell heterostructures. The synergistic effect of the as-synthesized $NaNbO_3$/CdS core/shell heterostructures enlarges the photoresponse of the band gap of $NaNbO_3$ and effectively retards the recombination of photogenerated charge carriers, thus finally inducing the UV-filtered visible light photocatalytic activity in $NaNbO_3$. Moreover, the core/shell heterostructures possesses admirable photostability and reusability even after three consecutive cycles of degradation. Our findings evince that the control of morphological design and appropriate band alignment should be the main thrust of photocatalyst design. We envision that our results open up a new avenue for exploring novel core/shell

heterostructures for environmental remediation and energy-harvesting applications.

■ ASSOCIATED CONTENT

Supporting Information

Figure S1: TEM image of CdS nanoparticles. Figure S2: Nitrogen adsorption−desorption isotherms of the uncoated $NaNbO_3$ nanorods. Figure S3: TEM image of $NaNbO_3$/CdS core/shell heterostructures after 3 photocatalytic cycles. This material is available free of charge via the Internet at http://pubs.acs.org.

■ AUTHOR INFORMATION

Corresponding Author

*E-mail: ashok@chemistry.iitd.ernet.in. Tel No. 91-11-26591511. Fax 91-11-26854715.

Notes

The authors declare no competing financial interest.

■ ACKNOWLEDGMENTS

A.K.G. and M.T. thank Department of Science & Technology (DST) and Council of Scientific and Industrial Research (CSIR), Govt. of India for financial support. Sandeep Kumar and Sunita Khanchandani thank DST and CSIR, Govt. of India for a fellowship, respectively.

■ REFERENCES

(1) Hoffmann, M. R.; Martin, S. T.; Choi, W.; Bahnemannt, D. W. Environmental Applications of Semiconductor Photocatalysis. *Chem. Rev.* **1995**, *95*, 69−96.

(2) Serpone, N.; Emeline, A. V. Semiconductor Photocatalysis−Past, Present, and Future Outlook. *J. Phys. Chem. Lett.* **2012**, *3*, 673−677.

(3) Fujishima, A.; Honda, K. Electrochemical Photolysis of Water at a Semiconductor Electrode. *Nature* **1972**, *238*, 37−38.

(4) Zhang, L.; Yin, L.; Wang, C.; Lun, N.; Qi, Y. Sol-Gel Growth of Hexagonal Faceted ZnO Prism Quantum Dots with Polar Surfaces for Enhanced Photocatalytic Activity. *ACS Appl. Mater. Interfaces* **2010**, *2*, 1769−1773.

(5) Manjula, P.; Boppella, R.; Manorama, S. V. A Facile and Green Approach for the Controlled Synthesis of Porous SnO_2 Nanospheres: Application as an Efficient Photocatalyst and an Excellent Gas Sensing Material. *ACS Appl. Mater. Interfaces* **2012**, *4*, 6252−6260.

(6) Dunkle, S. S.; Helmich, R. J.; Suslick, K. S. $BiVO_4$ as a Visible−Light Photocatalyst Prepared by Ultrasonic Spray Pyrolysis. *J. Phys. Chem. C* **2009**, *113*, 11980−11983.

(7) Kuang, Q.; Yang, S. Template Synthesis of Single-Crystal-like Porous $SrTiO_3$ Nanocube Assemblies and Their Enhanced Photocatalytic Hydrogen Evolution. *ACS Appl. Mater. Interfaces* **2013**, *5*, 3683−3690.

(8) Li, P.; Ouyang, S.; Xi, G.; Kako, T.; Ye, J. The Effects of Crystal Structure and Electronic Structure on Photocatalytic H_2 Evolution and CO_2 Reduction over Two Phases of Perovskite-Structured $NaNbO_3$. *J. Phys. Chem. C* **2012**, *116*, 7621−7628.

(9) Nanda, K. K.; Swain, S.; Satpati, B.; Besra, L.; Chaudhary, Y. S. Facile Synthesis and the Photo-catalytic Behavior of Core−Shell Nanorods. *RSC Adv.* **2014**, *4*, 10928−10934.

(10) Zheng, H.; Liu, K.; Cao, H.; Zhang, X. L−Lysine-Assisted Synthesis of ZrO_2 Nanocrystals and Their Application in Photocatalysis. *J. Phys. Chem. C* **2009**, *113*, 18259−18263.

(11) Wang, F.; Di Valentin, C.; Pacchioni, G. Rational Band Gap Engineering of WO_3 Photocatalyst for Visible Light Water Splitting. *ChemCatChem* **2012**, *4*, 476−478.

(12) Yu, K.; Yang, S.; Liu, C.; Chen, H.; Li, H.; Sun, C.; Boyd, S. a. Degradation of Organic Dyes via Bismuth Silver Oxide Initiated Direct Oxidation Coupled with Sodium Bismuthate Based Visible Light Photocatalysis. *Environ. Sci. Technol.* **2012**, *46*, 7318−7326.

(13) Tang, J.; Zou, Z.; Ye, J. Efficient Photocatalysis on $BaBiO_3$ Driven by Visible Light. *J. Phys. Chem. C* **2007**, *114*, 12779−12785.

(14) Kim, H. G.; Hwang, D. W.; Lee, J. S. An Undoped, Single−Phase Oxide Photocatalyst Working under Visible Light. *J. Am. Chem. Soc.* **2004**, *126*, 8912−8913.

(15) Wang, X.; Chen, G.; Zhou, C.; Yu, Y.; Wang, G. N−Doped Nb_2O_5 Sensitized by Carbon Nitride Polymer − Synthesis and High Photocatalytic Activity under Visible Light. *Eur. J. Inorg. Chem.* **2012**, *2012*, 1742−1749.

(16) Li, G.; Yi, Z.; Bai, Y.; Zhang, W.; Zhang, H. Anisotropy in Photocatalytic Oxidization Activity of $NaNbO_3$ Photocatalyst. *Dalton Trans.* **2012**, *41*, 10194−10198.

(17) Shi, H.; Li, X.; Wang, D.; Yuan, Y.; Zou, Z.; Ye, J. $NaNbO_3$ Nanostructures: Facile Synthesis, Characterization, and Their Photocatalytic Properties. *Catal. Lett.* **2009**, *132*, 205−212.

(18) Lv, J.; Kako, T.; Li, Z.; Zou, Z.; Ye, J. Synthesis and Photocatalytic Activities of $NaNbO_3$ Rods Modified by In_2O_3 Nanoparticles. *J. Phys. Chem. C* **2010**, *114*, 6157−6162.

(19) Li, G.; Yang, N.; Wang, W.; Zhang, W. F. Synthesis, Photophysical and Photocatalytic Properties of N-Doped Sodium Niobate Sensitized by Carbon Nitride. *J. Phys. Chem. C* **2009**, *113*, 14829−14833.

(20) Li, P.; Xu, H.; Liu, L.; Kako, T.; Umezawa, N.; Abe, H.; Ye, J. Constructing Cubic−Orthorhombic Surface-Phase Junctions of $NaNbO_3$ towards Significant Enhancement of CO_2 Photoreduction. *J. Mater. Chem. A* **2014**, 5606−5609.

(21) Shifu, C.; Lei, J.; Wenming, T.; Xianliang, F. Fabrication, Characterization and Mechanism of a Novel Z−Scheme Photocatalyst $NaNbO_3$/WO_3 with Enhanced Photocatalytic Activity. *Dalton Trans.* **2013**, *42*, 10759−10768.

(22) Xu, H.; Liu, C.; Li, H.; Xu, Y.; Xia, J.; Yin, S.; Liu, L.; Wu, X. Synthesis, Characterization and Photocatalytic Activity of $NaNbO_3$/ZnO Heterojunction Photocatalysts. *J. Alloys Compd.* **2011**, *509*, 9157−9163.

(23) Chen, S.; Hu, Y.; Ji, L.; Jiang, X.; Fu, X. Preparation and Characterization of Direct Z−Scheme Photocatalyst Bi_2O_3/$NaNbO_3$ and Its Reaction Mechanism. *Appl. Surf. Sci.* **2014**, *292*, 357−366.

(24) Xia, Y.; Yang, P.; Sun, Y.; Wu, Y.; Mayers, B.; Gates, B.; Yin, Y.; Kim, F.; Yan, H. One-Dimensional Nanostructures: Synthesis, Characterization, and Applications. *Adv. Mater.* **2003**, *15*, 353−389.

(25) Weng, B.; Liu, S.; Tang, Z.-R.; Xu, Y.-J. One-Dimensional Nanostructure Based Materials for Versatile Photocatalytic Applications. *RSC Adv.* **2014**, *4*, 12685−12700.

(26) Reddy, K. H.; Martha, S.; Parida, K. M. Fabrication of Novel P−BiOI/n−$ZnTiO_3$ Heterojunction for Degradation of Rhodamine 6G under Visible Light Irradiation. *Inorg. Chem.* **2013**, *52*, 6390−6401.

(27) Rawal, S. B.; Bera, S.; Lee, D.; Jang, D.-J.; Lee, W. I. Design of Visible−Light Photocatalysts by Coupling of Narrow Bandgap Semiconductors and TiO_2: Effect of Their Relative Energy Band Positions on the Photocatalytic Efficiency. *Catal. Sci. Technol.* **2013**, *3*, 1822−1830.

(28) Zhang, Z.; Wang, W.; Wang, L.; Sun, S. Enhancement of Visible−Light Photocatalysis by Coupling with Narrow-Band-Gap Semiconductor: A Case Study on Bi_2S_3/Bi_2WO_6. *ACS Appl. Mater. Interfaces* **2012**, *4*, 593−597.

(29) Kamat, P. V. Quantum Dot Solar Cells. The Next Big Thing in Photovoltaics. *J. Phys. Chem. Lett.* **2013**, *4*, 908−918.

(30) Nozik, A. J.; Beard, M. C.; Luther, J. M.; Law, M.; Ellingson, R. J.; Johnson, J. C. Semiconductor Quantum Dots and Quantum Dot Arrays and Applications of Multiple Exciton Generation to Third-Generation Photovoltaic Solar Cells. *Chem. Rev.* **2010**, *110*, 6873−6890.

(31) Yang, Y.; Rodríguez-Córdoba, W.; Lian, T. Multiple Exciton Generation and Dissociation in PbS Quantum Dot-Electron Acceptor Complexes. *Nano Lett.* **2012**, *12*, 4235−4241.

(32) Beard, M. C. Multiple Exciton Generation in Semiconductor Quantum Dots. *J. Phys. Chem. Lett.* **2011**, *2*, 1282−1288.

(33) Hu, Y.; Liu, Y.; Qian, H.; Li, Z.; Chen, J. Coating Colloidal Carbon Spheres with CdS Nanoparticles: Microwave-Assisted Syn-

thesis and Enhanced Photocatalytic Activity. *Langmuir* **2010**, *26*, 18570−18575.
(34) Jing, D.; Guo, L. Efficient Hydrogen Production by a Composite CdS/Mesoporous Zirconium Titanium Phosphate Photocatalyst under Visible Light. *J. Phys. Chem. C* **2007**, *111*, 13437−13441.
(35) Barpuzary, D.; Qureshi, M. Enhanced Photovoltaic Performance of Semiconductor−Sensitized ZnO−CdS Coupled with Graphene Oxide as a Novel Photoactive Material. *ACS Appl. Mater. Interfaces* **2013**, *5*, 11673−11682.
(36) Li, G. S.; Zhang, D. Q.; Yu, J. C. A New Visible−Light Photocatalyst: CdS Quantum Dots Embedded Mesoporous TiO_2. *Environ. Sci. Technol.* **2009**, *43*, 7079−7085.
(37) Zhang, N.; Xu, Y.-J. Aggregation− and Leaching−Resistant, Reusable, and Multifunctional Pd@CeO_2 as a Robust Nanocatalyst Achieved by a Hollow Core−Shell Strategy. *Chem. Mater.* **2013**, *25*, 1979−1988.
(38) Tsai, S. H.; Chang, H. C.; Wang, H. H.; Chen, S. Y.; Lin, C. A.; Chen, S. A.; Chueh, Y. L.; He, J. H. Significant Efficiency Enhancement of Hybrid Solar Cells Using Core−Shell Nanowire Geometry for Energy Harvesting. *ACS Nano* **2011**, *5*, 9501−9510.
(39) Das, K.; De, S. K. Optical Properties of the Type−II Core−Shell TiO_2@CdS Nanorods for Photovoltaic Applications. *J. Phys. Chem. C* **2009**, *113*, 3494−3501.
(40) Wu, P.; Sun, T.; Dai, Y.; Sun, Y.; Ye, Y.; Dai, L. Novel Type−II Zn_3P_2/ZnO Core/Shell Nanowires: Synthesis, Characteristic, and Photoluminescence Properties. *Cryst. Growth Des.* **2011**, *11*, 1417−1421.
(41) Verma, S.; Kaniyankandy, S.; Ghosh, H. N. Charge Separation by Indirect Bandgap Transitions in CdS/ZnSe Type−II Core/Shell Quantum Dots. *J. Phys. Chem. C* **2013**, *117*, 10901−10908.
(42) Wang, Z.; Huang, B.; Dai, Y.; Qin, X.; Zhang, X.; Wang, P.; Liu, H.; Yu, J. Highly Photocatalytic ZnO/In_2O_3 Heteronanostructures Synthesized by a Coprecipitation Method. *J. Phys. Chem. C* **2009**, *113*, 4612−4617.
(43) Cheng, H.; Huang, B.; Dai, Y.; Qin, X.; Zhang, X. One-Step Synthesis of the Nanostructured AgI/BiOI Composites with Highly Enhanced Visible−Light Photocatalytic Performances. *Langmuir* **2010**, *26*, 6618−6624.
(44) Zhu, H.; Zheng, Z.; Gao, X.; Huang, Y.; Yan, Z.; Zou, J.; Yin, H.; Zou, Q.; Kable, S. H.; Zhao, J.; Xi, Y.; Martens, W. N.; Frost, R. L. Structural Evolution in a Hydrothermal Reaction between Nb_2O_5 and NaOH Solution: From Nb_2O_5 Grains to Microporous $Na_2Nb_2O_6.2/3H_2O$ Fibers and $NaNbO_3$ Cubes. *J. Am. Chem. Soc.* **2006**, *128*, 2373−2384.
(45) Oliveira, J. F. a.; Milão, T. M.; Araújo, V. D.; Moreira, M. L.; Longo, E.; Bernardi, M. I. B. Influence of Different Solvents on the Structural, Optical and Morphological Properties of CdS Nanoparticles. *J. Alloys Compd.* **2011**, *509*, 6880−6883.
(46) Kim, M. R.; Kang, Y.; Jang, D. Synthesis and Characterization of Highly Luminescent CdS@ZnS Core−Shell Nanorods. *J. Phys. Chem. C* **2007**, *111*, 18507−18511.
(47) Mukherjee, D.; Hordagoda, M.; Hyde, R.; Bingham, N.; Srikanth, H.; Witanachchi, S.; Mukherjee, P. Nanocolumnar Interfaces and Enhanced Magnetic Coercivity in Preferentially Oriented Cobalt Ferrite Thin Films Grown Using Oblique−Angle Pulsed Laser Deposition. *ACS Appl. Mater. Interfaces* **2013**, *5*, 7450−7457.
(48) Gautam, A.; Veggel, F. C. J. M. Van. Blue Electroluminescence from Eu^{2+} −Doped GaN @SiO_2 Nanostructures Tuned to Industrial Standards. *Chem. Mater.* **2011**, *23*, 4817−4823.
(49) Sippel, P.; Denysenko, D.; Loidl, A.; Lunkenheimer, P.; Sastre, G.; Volkmer, D. Dielectric Relaxation Processes, Electronic Structure, and Band Gap Engineering of MFU-4-Type Metal-Organic Frameworks:Towards a Rational Design of Semiconducting Microporous Materials. *Adv. Funct. Mater.* **2014**, *24*, 3885−3896.
(50) Mu, J.; Chen, B.; Zhang, M.; Guo, Z.; Zhang, P.; Zhang, Z.; Sun, Y.; Shao, C.; Liu, Y. Enhancement of the Visible−Light Photocatalytic Activity of In_2O_3−TiO_2 Nanofiber Heteroarchitectures. *ACS Appl. Mater. Interfaces* **2012**, *4*, 424−430.
(51) Kumar, S.; Chatterjee, S.; Chattopadhyay, K. K.; Ghosh, A. K. Sol−Gel-Derived ZnO:Mn Nanocrystals: Study of Structural, Raman, and Optical Properties. *J. Phys. Chem. C* **2012**, *116*, 16700−16708.
(52) Qin, W.; Szpunar, J. A. Origin of Lattice Strain in Nanocrystalline Materials. *Philos. Mag. Lett.* **2005**, *85*, 649−656.
(53) Peng, X.; Schlamp, M. C.; Kadavanich, A. V.; Alivisatos, A. P. Epitaxial Growth of Highly Luminescent CdSe/CdS Core/Shell Nanocrystals with Photostability and Electronic Accessibility. *J. Am. Chem. Soc.* **1997**, *119*, 7019−7029.
(54) Juang, Y. D.; Dai, S. B.; Wang, Y. C.; Chou, W. Y.; Hwang, J. S.; Hu, M. L.; Tse, W. S. Phase Transition of $Li_XNa_{1-X}NbO_3$ Studied by Raman Scattering Method. *Solid State Commun.* **1999**, *111*, 723−728.
(55) Xiao, M.; Wang, L.; Wu, Y.; Huang, X.; Dang, Z. Preparation and Characterization of CdS Nanoparticles Decorated into Titanate Nanotubes and Their Photocatalytic Properties. *Nanotechnology* **2008**, *19*, 015706−015713.
(56) Zhou, J.; Tian, G.; Chen, Y.; Shi, Y.; Tian, C.; Pan, K.; Fu, H. Growth Rate Controlled Synthesis of Hierarchical Bi_2S_3/In_2S_3 Core/shell Microspheres with Enhanced Photocatalytic Activity. *Sci. Rep.* **2014**, *4*, 4027.
(57) Huang, X.; Wang, M.; Willinger, M.-G.; Shao, L.; Su, D. S.; Meng, X.-M. Assembly of Three−Dimensional Hetero−Epitaxial ZnO/ZnS Core/Shell Nanorod and Single Crystalline Hollow ZnS Nanotube Arrays. *ACS Nano* **2012**, *6*, 7333−7339.
(58) Xiao, F.-X. Construction of Highly Ordered ZnO−TiO_2 Nanotube Arrays (ZnO/TNTs) Heterostructure for Photocatalytic Application. *ACS Appl. Mater. Interfaces* **2012**, *4*, 7055−7063.
(59) Yang, M.−Q.; Xu, Y.−J. Basic Principles for Observing the Photosensitizer Role of Graphene in the Graphene−Semiconductor Composite Photocatalyst from a Case Study on Graphene−ZnO. *J. Phys. Chem. C* **2013**, *117*, 21724−21734.
(60) Shi, Y.; Li, H.; Wang, L.; Shen, W.; Chen, H. Novel α−Fe_2O_3/CdS Cornlike Nanorods with Enhanced Photocatalytic Performance. *ACS Appl. Mater. Interfaces* **2012**, *4*, 4800−4806.
(61) Vinodgopal, K.; Bedja, I.; Kamat, P. V. Nanostructured Semiconductor Films for Photocatalysis. Photoelectrochemical Behavior of SnO_2/TiO_2 Composite Systems and Its Role in Photocatalytic Degradation of a Textile Azo Dye. *Chem. Mater.* **1996**, *8*, 2180−2187.
(62) Chatterjee, S.; Tyagi, A. K.; Ayyub, P. Efficient Photocatalytic Degradation of Rhodamine B Dye by Aligned Arrays of Self-Assembled Hydrogen Titanate Nanotubes. *J. Nanomater.* **2014**, *2014*, 1−7.
(63) Forgacs, E.; Cserháti, T.; Oros, G. Removal of Synthetic Dyes from Wastewaters: A Review. *Environ. Int.* **2004**, *30*, 953−971.
(64) Senthilkumaar, S.; Porkodi, K.; Gomathi, R.; Geetha Maheswari, A.; Manonmani, N. Sol−gel Derived Silver Doped Nanocrystalline Titania Catalysed Photodegradation of Methylene Blue from Aqueous Solution. *Dyes Pigm.* **2006**, *69*, 22−30.
(65) Fu, H.; Pan, C.; Yao, W.; Zhu, Y. Visible−Light−Induced Degradation of Rhodamine B by Nanosized Bi_2WO_6. *J. Phys. Chem. B* **2005**, *109*, 22432−22439.
(66) Lv, J.; Kako, T.; Zou, Z.; Ye, J. Band Structure Design and Photocatalytic Activity of In_2O_3/N−$InNbO_4$ Composite. *Appl. Phys. Lett.* **2009**, *95*, 032107−03210.
(67) Wang, Y.; Deng, K.; Zhang, L. Visible Light Photocatalysis of BiOI and Its Photocatalytic Activity Enhancement by in Situ Ionic Liquid Modification. *J. Phys. Chem. C* **2011**, *115*, 14300−14308.